Identifying mechanisms of shore platform erosion using Structure-from-Motion (SfM) photogrammetry

Zuzanna M. Swirad, Nick J. Rosser, Matthew J. Brain

Department of Geography, Durham University, South Road, Durham, DH1 3LE, UK

z.m.swirad@durham.ac.uk

Abstract

Shore platforms control wave energy transformation which, in turn, controls energy delivery to the cliff toe and nearshore sediment transport. Insight into shore platform erosion rates has conventionally been constrained at mm-scales using micro-erosion metres, and at m-scales using cartographic data. On apparently slowly eroding coasts, such approaches are fundamentally reliant upon long-term observation to capture emergent erosion patterns. Where in practise timescales are short, and where change is either below the resolution or saturates the mode of measurement, the collection of data that enables the identification of the actual mechanisms of erosion is hindered.

We developed a method to monitor shore platform erosion at millimetre resolution within metre-scale monitoring plots using Structure-from-Motion photogrammetry. We conducted monthly surveys at 15 0.25 m^2 sites distributed across the Hartle Loup platform in North Yorkshire, UK, over one year. We derived topographic data at 0.001 m resolution, retaining a vertical precision of change detection of 0.001 m. We captured a mean erosion rate of 0.528 mm yr^{-1}, but this varied considerably both across the platform and through the year. We characterised the volume and shape of

This article has been accepted for publication and undergone full peer review but has not been through the copyediting, typesetting, pagination and proofreading process which may lead to differences between this version and the Version of Record. Please cite this article as doi: 10.1002/esp.4591

eroded material. The detachment volume-frequency and shape distributions suggest that erosion happens primarily via removal of shale platelets. We identify that the at-a-point erosion rate can be predicted by the distance from the cliff and the tidal level, whereby erosion rates are higher closer to the cliff and at locations of higher tidal duration. The size of individual detachments is controlled by local micro-topography and rock structure, whereby larger detachments are observed on more rough sections of the platform. Faster erosion rates and larger detachments occur in summer months, rather than in more energetic winter conditions. These results have the potential to form the basis of improved models of how platforms erode over both short- and long-timescales.

Keywords: bedrock erosion, micro-erosion, down-wearing, shore platforms, rocky coasts, Structure-from-Motion

Introduction

The erosion of shore platforms is central to understanding the dynamics of rocky coasts because they control wave energy dissipation, energy delivery to cliffs and enable or inhibit sediment transport (Dickson et al., 2013; Ogawa et al., 2016; Poate et al., 2018). Shore platforms are understood to erode via a combination of incremental down-wearing and lateral erosion of ‘steps’ (Figure 1A; Stephenson, 2000). This dichotomy in scales of erosion arguably in part reflects the techniques conventionally used to detect geomorphic change on foreshores. Monitoring sub-millimetre down-wearing rates with micro-erosion metres (MEMs) captures grain-scale changes, such as those arising from abrasion (Robinson, 1976; 1977; Stephenson and Kirk, 1998; 2001), while historical maps and aerial photographs

allow the landward retreat of steps to be measured (Dornbusch and Robinson, 2011). There is a gap in our understanding of how observed erosion rates can be up- and down-scaled, and the spatio-temporal scales at which processes dominate landscape evolution remain poorly constrained.

The two erosion processes – down-wearing and step back-wearing – are represented in models simulating coastal evolution (e.g. Kline et al., 2014; Limber et al., 2014; Matsumoto et al., 2016), and in models that reconstruct past cliff retreat by estimating foreshore cosmogenic isotope concentrations (e.g. Choi et al., 2012; Regard et al., 2012; Hurst et al., 2016, 2017). These models necessarily simplify platform morphology and treat erosion implicitly, by enforcing either a single down-wearing rate derived from cliff retreat rates, or a set of elevation-dependent values related to tidally-dependent wave energy dissipation (Trenhaile, 1983; 2000; Walkden and Hall, 2005; Kline et al., 2014; Limber et al., 2014).

The complexity of platform morphology, and the observational evidence of foreshore erosion processes, suggests that simplified models of platform erosion may be insufficient. These models may not fully describe the broad range of processes driving change or, perhaps most importantly, the temporal and spatial scales over which these processes occur (Figure 1B). Significant insight has, however, been made at the micro-scale where the following key mechanisms of erosion have been identified: 1) grain-by-grain abrasion (Kirk, 1977; Blanco-Chao et al., 2007); and 2) fragmentation of rock facilitated by wetting and drying (Robinson, 1977; Stephenson and Kirk, 1998), warming and cooling (Coombes, 2014; Mayaud et al., 2014), salt crystallisation in rock lattices (Mottershead, 1989; Stephenson and Kirk, 2001) and biological activity (Andrews and Williams, 2000; Naylor et al., 2012), followed by removal of fragments via hydraulic drag-and-lift force, grain wedging

(Kirk, 1977; Stephenson and Kirk, 2001; Blanco-Chao et al., 2007) and impacts (Cullen and Bourke, 2018). The rate of platform down-wearing has been shown to be controlled by: 1) rock type (Kirk, 1977; Stephenson and Kirk, 1998; Taylor, 2003; Dasgupta, 2010; Moura et al., 2011); 2) elevation with respect to tidal duration distribution (frequency of submergence/emergence transitions) which is observed to link erosion rate to direct wave action (Robinson, 1977; Foote et al., 2006), wetting and drying (Kirk, 1977; Robinson, 1977; Stephenson and Kirk, 1998) and biological activity (Torunski, 1979); 3) slope (Robinson, 1977); 4) rock structure (Swantesson et al., 2006); 5) the presence or absence of beach deposits (Robinson, 1977); and 6) biological cover (Coombes et al., 2017). Erosion rates change through time, with higher rates observed either in summer when higher temperatures increase efficiency of thermal expansion of salt crystals, and wetting and drying (Robinson, 1977; Mottershead, 1989; Stephenson and Kirk, 1998; 2001), or in winter as a result of increased storminess and wave energy delivery to the foreshore (Robinson, 1977; Foote et al., 2006; Moses and Robinson, 2011). Although a range of processes of erosion have been identified, the relative contribution of these time- and space-variable processes to erosion and, in turn, coastal change remains poorly constrained.

Measuring erosion rates at a wider range of spatial scales (from 10^{-3} to 10^{-1} m; Figure 2) relative to MEM and point-based measurements remains challenging with conventional monitoring methods, which tend to be precise but highly localised (e.g. MEMs), or 1D or 2D rather than 3D (e.g. pin-frames). Recent advances in Structure-from-Motion (SfM) photogrammetry, where topography across a range of scales can be reconstructed from uncalibrated photography (Westoby et al., 2012; Cook, 2017; Turowski and Cook, 2017), presents an alternative approach, providing

continuous measurement across a surface and allowing the assessment of the 3D geometry of detachments. SfM is also better suited for monitoring horizontal surfaces at close range than terrestrial laser scanning (TLS) (Smith, 2015), as the approach minimises topographic occlusion that arises from a single instrument position. The flexibility in the scale at which SfM is applied on foreshores has the potential to bridge the gap between the point MEM measurements and the metre-scale monitoring from cartographic sources.

Although SfM has been recently widely used to reconstruct topography, it has been used less often to monitor change. Cook et al. (2017) compared change detected using SfM and TLS, highlighting the importance of the specific nature of the monitored topography on SfM performance. James et al. (2017) proposed using a map of 3D precision to decrease the uncertainty of detected change. Cullen et al. (2018) concluded that SfM can be successfully used to monitor sub-mm to cm bedrock erosion of low-roughness surfaces. The relative scarcity of studies that use SfM methods to monitor topographic change is due to a number of factors which influence the performance of the approach which remain difficult to control, including lighting conditions, camera position, surface reflectivity, texture and roughness (Rock et al., 2011; Nitsche et al., 2013; Gonçaves and Henriques, 2015; Cook, 2017), many of which can change between survey epochs introducing false change. Sources of error such as camera distortion are, however, relatively well understood and techniques to quantify them and minimise their influence have been developed (Wackrow et al., 2007; Wackrow and Chandler, 2008; Cook, 2017; Marteau et al., 2017).

We present the results of a year of monthly SfM monitoring of a set of shore platform erosion plots distributed across a macro-tidal foreshore. Our aim is to identify spatial and temporal patterns of micro-scale (10^{-3} – 10^{-2} m) erosion in order to constrain the dominant mechanisms of shore platform erosion and identify the key controls on the size distribution of eroded material. To do so, we have built on existing SfM techniques to develop a method capable of detecting erosion at scales relevant to shore platform erosion.

Study site

The Hartle Loup shore platform is located immediately east of Staithes, North Yorkshire, UK (Figure 3). The coast is storm-dominated with a macro-tidal spring tide range of 4.6 m and a neap tide range of 2.25 m (http://www.ntslf.org/). The ~60 m high adjacent Penny Nab cliff is composed of sedimentary Jurassic rocks (mudstones, sandstones and shales), overlain by 10 to 20 m of glacial till (Rawson and Wright, 2000). The mean cliff retreat rate along this coast is 0.027 ± 0.029 m yr^{-1} (Rosser et al., 2013).

The Hartle Loup platform is 320 m wide, north facing, with an average 2° seaward slope. The platform is formed in Jurassic shale and sandstone with a 2° north-south trending dip. The platform is composed of four main bedrock exposures which each terminate with abrupt breaks in slope, henceforth referred to as ‘steps’. Discontinuities (joints and faults) of a range of scales dissect the platform surface (Figure 2B). In general, the surface is at higher elevation and is steeper closer to the cliff toe. The platform surface is characterised by a heterogeneous cover of intertidal algae and patches of barnacles, which are typically found in topographic lows that retain water during low tides, and on the most seaward portions of the platform which

are less frequently exposed (Figure 3D). Closer to the cliff toe the algae and barnacle cover becomes more sparse, concentrating in niches, included joints and rock pools (Figure 2B) (Swirad et al., 2016).

Evidence of meso-scale (10^{-1} – 10^{0} m) erosion via block removal (Naylor and Stephenson, 2010; Stephenson and Naylor, 2011) is manifest by the presence of angular boulders in front of (downslope) steps (Figure 2A), while the smaller-scale erosion (10^{-2} m) is apparent as fresh, apparently-broken rock (Figure 2 C and D). The surface-parallel micro-scale laminated structure of the sedimentary rocks gives the platform surface, and apparently the detachments which it releases, a platy structure, with individual detachments ≤ 0.02 m in length.

In one of the first studies of shore platform erosion rates, Robinson (1977) monitored platform down-wearing along the same 35 km North Yorkshire coastline using a MEM. Robinson (1977) calculated erosion rates using 70 sites clustered in nine alongshore locations at two-month intervals over two years. The down-wearing rate varied between -1.50 mm yr^{-1} (i.e. surface swelling) and 19.31 mm yr^{-1} with an average of 3.21 ± 4.76 mm yr^{-1}. In general, greater erosion rates of 5.20 ± 5.87 mm yr^{-1} were observed on the landward sections of the platform, termed cliff-proximal ramps (~15° steep), than on the low-gradient seaward section with erosion rates of 1.33 ± 2.17 mm yr^{-1} (Robinson, 1977).

Methods

Monitoring shore platform erosion with Structure-from-Motion

For our study, we aimed to bridge the gap between the sub-millimetre point-based measurements obtained by, for example, Robinson (1977) and the metre-scale studies using cartographical data (e.g. Dornbusch and Robinson, 2011). Based upon observations of the apparent nature of detachments (micro-structurally defined platelets of 0.010 - 0.015 m major axis length), we designed our monitoring to capture detachments of at least this scale and ideally one order of magnitude smaller, across an area likely to generate large numbers of detachments to enable statistical analysis of their character (volume and shape), and key controls thereon. After testing the practicalities of the image capture set-up in the laboratory, we selected a plot with dimensions 0.5 × 0.5 m and a target spatial resolution for the resulting digital elevation model of 0.001 m. We found that a minimum of six photographs were needed to be able to resolve 0.001 m of vertical change over the area of interest and to minimise occlusion from an image capture height of ~0.9 m (see Supplementary Material).

We mounted six Canon EOS 1200D cameras (18 MP, 18-55 mm lens) to a rigid aluminium frame, each at a 0.9 m height (Figure A2 in Supplementary Material). Camera positions, orientations and numbers were fixed to maintain the consistency of occlusion effects and to enable comparison between elevation models through time. Eight retroreflective markers imaged by every camera were mounted on the frame, and served as the Ground Control Points (CGPs) (6) and as independent Check Points (CPs) (2) after Marteau et al. (2017). We calculated the relative coordinates (x,y) of the markers assuming constant z values relative to the local coordinate system (see Supplementary Material). One frame leg had a locating pin

that was located within a shoe on a survey bolt installed at each monitoring site, which combined with a compass allowed repositioning (± 2°). Extraneous surface debris and standing water were removed prior to photography. A white cloth enclosed the frame to maintain broadly similar lighting conditions throughout the monitoring.

We selected 15 sites (Figure 3C) that were chosen to encompass a range of elevations, rock types, rock-surface joint densities and morphology; we aimed to identify and consider factors affecting erosion rates using this sampling approach, rather than systematically obtaining data across the entire platform (Table 1). We surveyed all sites on 13 occasions between April 2016 and April 2017 (total period: 370 days = 1.01 years) at approximately equal intervals (24 to 43 days, average 30.8 days), as and when tide and weather conditions allowed.

Calculating erosion rates

We built point clouds with a point density on the surface of 7.20 ± 0.31 points mm^{-2} using Agisoft PhotoScan Professional 1.2.4 (photo alignment settings: high accuracy, generic pair preselection; high quality dense cloud; point export with precision = 6). To precisely position each survey, data were nested within georeferenced point clouds captured with an Unmanned Aerial Vehicle (UAV) and positioned with dGPS, whereby individual plot data were precisely positioned using iterative closest-point alignment (see Supplementary Material).

We converted the point clouds into georeferenced Digital Elevation Models (DEMs) and ortho-photomaps with 0.001 m resolution using kriging of the average point elevation (ENVI Classic 5.1), within the OSGB02 coordinate system. To quantify erosion, we extracted the difference between successive DEMs. Upon

inspection, a doming effect was identified in some datasets, as reported previously elsewhere (e.g. Wackrow et al., 2007; Wackrow and Chandler, 2008). To compensate for this, DoD surfaces were detrended by subtracting an image generated using a low-pass filter (mean elevation with a square 2,601-pixel neighbourhood, equivalent to 10% of the monitoring plot width) from each DoD. We converted change ≥ 0.001 m into a polygonal shapefile to define the planform geometry of each detachment. We used the ortho-photographs of the surveys preceding each time period to remove polygons occupied by algae and animals. We assumed that an area of change in a single epoch was a single detachment, rather than superimposed or coalesced events. As initial assessment of the results revealed that objects less than 6 pixels (6.00×10^{-6} m^2) in size could not be distinguished from noise, these data were removed from analysis. We then performed a set of experiments to identify further potentially erroneous objects, based upon a standardised set of geometrical criteria that filtered out and removed physically-implausible detachment shapes (see Supplementary Material).

The resulting inventory of detachments was attributed with location, date, site characteristics and object-specific metrics, including measured eroded planform area (m^2) and detached volume (m^3). For each site the eroded area, *Area* (m^2), and the total detached volume, *Vol* (m^3), were used to derive the erosion rate, *Ero* (mm yr^{-1}), calculated as:

$$Ero = 1000 \frac{Vol}{(\frac{AOI}{t})} \quad (1)$$

where *AOI* = 0.25 m^2, as the total surface area of interest, and *t* = 1.01 yr, as the duration of the monitoring period. We summarised the size of detachments using the mean volume, *Mean* (m^3), and the standard deviation of volumes, *Std* (m^3) (Table 2).

We summarised total eroded volume and average volume lost per 1 m^2, but we used down-wearing rates (mm yr^{-1}) in the discussion to enable direct comparison with existing MEM studies.

Constraining the mechanisms and controls on erosion

We analysed the volume, frequency and shape characteristics of detachments, adapting a suite of analyses from research on landslides and rockfalls (e.g. Dussauge-Peisser et al., 2002; Malamud et al., 2004; Williams et al, 2018). The relationship between detachment area, *Area* (m^2), and volume, *Vol* (m^3), is assumed to be represented as:

$$Vol = a\ Area^b \tag{2}$$

where *a* is a constant and *b* is the power-law exponent. The fit to, and deviation from, the power law can be used to explore the possibility of scale-invariant behaviour, or changes in mechanism as a function of volume (Guzetti et al., 2009; Larsen et al., 2010; Williams et al., 2018). Similarly, the relationship between the magnitude and frequency of detachment volume can provide valuable insight into the nature of detachments observed, as is described by the power law using least-squares fitting (after Clauset et al., 2009) as:

$$f = \alpha\ Vol^{-\beta} \tag{3}$$

where *f* is the non-cumulative frequency, α is a constant and β is the volume-frequency power-law exponent. This exponent describes the size distribution of events, with a higher value indicating higher proportion of smaller events in the overall inventory (Malamud et al., 2004). We hypothesised that the 3D shape of detachments from the shore platform could indicate either a specific mechanism of erosion, or might reflect micro-structural controls on erosion style. We assessed the

3D shapes of the detachments using the ternary plot designed by Sneed and Folk (1958) for sedimentological studies, and adapted to rock studies by Kalenchuk et al. (2006).

We developed regression models to predict three erosion variables in our monitoring sites: the erosion rate, *Ero* (mm yr^{-1}), the mean detachment volume, *Mean* (m^3), and the non-cumulative volume-frequency exponent *β*, using 12 independent variables which describe location on the platform, topography at the macro- and micro-scales, tidal properties and jointing (Tables 1 and 2). The macro-scale topography variables – elevation, *Ele* (m AOD), slope, *Slo* (°), and roughness, *Rou* (°) – are obtained from a wider area LiDAR dataset (ca. 50 points m^{-2}) acquired on 8 April 2016 (see Benjamin et al., in review), whilst the micro-scale topography and jointing variables – curvature, *Cur*, site roughness, *SRou* (°), elevation range, *EleR* (m), number of joints, *JNo*, and length of joints, *JLe* (m) – are derived from the plot-based SfM analysis. We used 12 sites as a training set to develop the model, which we then tested on the remaining three sites (12, 13 and 15), selected to encompass sufficiently diverse morphologies and rock types. Instead of using an automated procedure to select a combination of variables which provides the best-fit linear model, we manually constructed the multiple regression models to account for physical meaning rather than goodness-of-fit only (e.g. Parker et al., 2015).

Results

Net erosion rate

The one-year monitoring of shore platform erosion resulted in detection of a total of 28,756 discrete measurable detachments which cumulatively eroded 2.00 × 10^{-3} m^3 of bedrock, equivalent to the volume of a 0.126 m cube or a volume of 5.33 × 10^{-4} m^3 eroded from a 1 m^2 surface. The spatially and temporally averaged erosion rate is 5.28 × 10^{-4} m yr^{-1} (0.528 mm yr^{-1}).

Volume frequency, size and shape of detachments

A statistically-significant relationship (R^2 = 0.925, p < 0.05) was shown between the planform area of detachments and their volume. Although most detachments closely follow the fitted power-law trendline, a sub-population of events with proportionally larger volumes relative to their area is observed for smaller-area events. Two outliers are present for large area detachment sizes (Figure 4). The number of detachments decreases with increased volume (R^2 = 0.732, p < 0.05). The volume-frequency distribution curve has a complex shape with minor perturbations and a sharp break in the distribution slope at the detachment size equivalent to a 0.011 m cube, which is of an approximately equivalent scale to single shale platelets (Figure 5). To describe these apparent sub-populations, two additional trendlines were fitted for volumes larger and smaller than 1.26 × 10^{-6} m^3 excluding the roll-over at the smallest size range (< 1.12 × 10^{-8} m^3), with β = 0.926 (R^2 = 0.990, p < 0.05) for the detachments smaller than the threshold, and β = 2.534 (R^2 = 0.947, p < 0.05) for those larger (Figure 5). The detached material has a wide variety of shapes, though the highest frequency is of *very bladed* and *very platy* slab-like forms (Figure 6). The shapes appear to preferentially concentrate at particular

values (diagonal stripes in Figure 6), but this is explained by high numbers of events with planform size equal to the grid resolution and change precision, or a low multiple thereof.

Spatial and temporal distribution of erosion

Erosion varies considerably between the sites (Table 3). The total area (*Area*) varies between 0.015 m^2 at site 5 and 0.098 m^2 at site 3, which is equivalent to the erosion of 6.0 to 39.2%. The total volume (*Vol)* ranges between 2.56×10^{-5} m^3 at site 5 and 3.01×10^{-4} m^3 at site 3, and the erosion rate (*Ero*) between 0.101 mm yr^{-1} at site 5 and 1.192 mm yr^{-1} at site 3, indicating more than an order of magnitude difference in erosion rates between sites. This is also seen in the variability of the mean volume (*Mean*) and the standard deviation of volumes (*Std*) which span between 3.43×10^{-8} m^3 at site 2 and 1.14×10^{-7} m^3 at site 10, and 5.97×10^{-8} m^3 at site 2 and 4.52×10^{-7} m^3 at site 10, respectively. The volume-frequency exponent β varies between 0.555 at site 1 and 0.942 at site 15. Although site 3 is characterised by the highest rate of erosion (*Area*, *Vol* and *Ero*), detachments are generally the largest (*Mean*) and the volumes are the most diverse (*Std*) at site 10. Detachment shape shows no clear pattern when aggregated by site, but there is a dominance of detachments at the sandstone sites (1, 5 and 7) of *very platy*, *very bladed* and *very elongate* shape (Figure 6).

The period between 6th April and 2nd October 2016 was characterised by slightly higher rates of net erosion (0.576 mm yr^{-1}), contributing to 52% of the annual eroded volume, compared to the period of 2nd October 2016 to 11th April 2017 (0.497 mm yr^{-1}) (Figure 7). There is also greater variability in *Ero*, *Mean* and *Std* between the monitoring sites between April and October, while their highest values fall

between July and September. Between October and April, erosion rates averaged from the mean values per site are lower (*Ero* = 0.384 mm yr^{-1}), detachments are smaller (*Mean* = 4.43 × 10^{-8} m^3) and more consistent between (*Std* = 1.11 × 10^{-7} m^3), and the volume-frequency exponent is higher (β = 0.667) as opposed to the period between April and October with respective averaged values of *Ero* = 0.495 mm yr^{-1}, *Mean* = 8.40 × 10^{-8} m^3, *Std* = 2.16 × 10^{-7} m^3 and β = 0.480 (Figure 7).

Figure 8 summarises the spatial and temporal distribution of detachments across Hartle Loup as observed over the one-year monitoring program. Erosion rates are faster at sites closer to the cliff with the average *Ero* = 0.978 mm yr^{-1} at the three sites closest to the cliff and *Ero* = 0.309 mm yr^{-1} at the farthest three sites, and a greater volume of detachment occurs between April and October as compared to between October and April. The largest volume, yet lower-frequency detachments tend to concentrate at sites located closer to the cliff toe and occur primarily between April and October. Sandstone erodes slower as compared to shale (0.222 ± 0.122 and 0.682 ± 0.336 mm yr^{-1}, respectively), with rare but occasional large detachments.

Modelling controls on erosion

All independent variables except *Inu*, *EleR* and *JNo* contribute to best-fit models of erosion (Figure 9; Table 4). *Ero* is controlled by location on the platform, tidal duration, jointing and elevation which, excluding *JLe* can be obtained from a relatively low-resolution topography dataset and a tide-gauge record. However, because distances from the cliff and from the seaward edge are correlated with each other we excluded the former from the model so as not to overestimate importance of the cross-shore location. In consequence, the length of joints was excluded as it

does not increase performance of the model when the distance from the cliff is ignored. *Ero* is higher farther from the seaward edge (higher *Sea*) and at the locations with higher *Tid* i.e. where the tide cycles more frequently (R^2 = 0.648, p < 0.05). Detachments are larger (higher *Mean)* at more rough surfaces (higher *SRou*) with lower gradient (lower *Slo*) which are located closer to the cliff (lower *Cli*) (R^2 = 0.734, p < 0.05). Exponent β negatively correlates with *SRou* which means that at more rough surfaces larger detachments dominate. In comparison to other erosion variables this relationship is weak yet still significant (R^2 = 0.457, p < 0.05). There is limited structure in the residual distribution, confirmed by Shapiro-Wilk tests that show that the residuals of erosion variables have normal distributions (5% significance level) when the test site 12 is excluded (Figure 10).

Discussion

We developed a method to monitor bedrock erosion at the 10^{-3} – 10^{-1} m scale using SfM. The method allowed us to consider a wider variety of spatial scales, rock structures and surface relief and features than previously obtainable in foreshore studies. In turn, this enabled us to better constrain the mechanisms of erosion through analysis of detachment size and shape and to improve understanding of controls on erosion on the basis of the character and spatial and temporal distribution of detachments.

Erosion rates

Our calculated mean erosion rate of 0.528 mm yr^{-1} is lower than the global mean shore platform erosion rates of 1.486 mm yr^{-1} (Stephenson and Finlayson, 2009) and 1.148 mm yr^{-1} (Dasgupta, 2010). The relatively high global erosion rates

may be caused by over-representation of studies focused on quickly-eroding chalk platforms (Andrews and Williams, 2000; Foote et al., 2006; Dornbusch et al., 2006). Our results are, however, comparable with values of 0.20 to 2.80 mm yr^{-1} of down-wearing of shale platforms in the Algarve, Portugal (Andrade et al., 2002), and values of 0.94 ± 1.20 mm yr^{-1} of down-wearing of sandstone platforms in Bay of Fundy, Canada (Porter and Trenhaile, 2007). This suggests a broader rock control, where erosion rates average out despite different approaches.

The calculated mean erosion rate we report is one order of magnitude lower than that recorded along the same coast by Robinson (1977), despite the shore platforms under examination having broadly equivalent lithology, tidal range and exposure to storm conditions. The difference in calculated erosion rates may be in part associated with the method employed to measure erosion. Firstly, we filter out change < 0.001 m, while at 40% (28) of single sites Robinson (1977) measured change below this threshold. Secondly, Robinson (1977) relied on the point measurements of the surface elevation change, whereas we measure net erosion by spatially averaging across a wider area using a raster-based detachment inventory. Robinson (1977) calculated the mean erosion rates on the basis of 210 point readings – three points from each of the 70 MEM stations – for a 35 km stretch of coastline. Use of a continuous raster allowed us extract the equivalent of 3.75×10^6 single point values (here pixels), equivalent to a grid of 500 × 500 pixels for the 15 monitoring sites located on a single platform (distance between the farthest sites 7 and 14 = 217.65 m). The procedure used here resulted in filtering out pixels with the vertical change < 0.001 m, as this was deemed indistinguishable from noise, and accepting objects that met specific size and shape criteria as ‘true’ detachments. Therefore, our erosion rates are calculated on the basis of a pixel sub-population,

while Robinson (1977) generated mean values based on point measurements. Our approach is less sensitive to individual or low numbers of spurious measurements, or large single at-a-point elevation changes. The results suggest that point-based erosion measurements may not be suitable for extrapolation and application in coastal evolution models because they hide spatial variability.

Mechanisms of erosion

We explored the geometry of detachments to consider the likely mechanisms of erosion, such as single discrete-platelet detachment versus grain-by-grain erosion. The strong relationship between measured detachment planform area and the volume (Figure 4) indicates a largely scale-invariant characteristic shape of detachments from the shore platform. This implies either a single dominant mechanism of erosion that operates across a range of scales, or that a range of erosion processes each result in detachment shapes that are themselves pre-defined, most probably by rock micro-structure. The area volume exponent *b* can be indicative of underlying erosion mechanism and is higher (> 1.2-1.3) for relatively deep detachments related to shear stresses acting along shear planes (Guzetti et al., 2009; Larsen et al., 2010) and lower where near-surface tensile stresses dominate erosion (Rosser et al., 2007; Williams et al., 2018). On this basis, our results (*b* = 1.125) suggest that tensile failure causes fracture and platelet detachment assuming the relationships hold across scales (Figure 11). With high moments imposed by hydraulic pressure gradients, or impact pressures on the shore platform surface, it may be relatively easy to remove rock fragments, but this remains difficult to capture directly. However, the rock type and water/sediment dynamics at the foreshore suggest that the rock micro-structure and the spatially-

variant compressive, shear and tensile stresses make the erosion process fundamentally complicated. This suggests that a single assessment of rock strength, such as that provided by a Schmidt hammer or Equotip device (see e.g. Viles et al., 2011) may be insufficient in providing a measurement of rock strength that is appropriate in understanding a range of detachment processes. As such, using a single value of rock strength as a predictor of erosion rate (Trenhaile, 1983; 2000; Walkden and Hall, 2005; Kline et al., 2014) is unlikely to be valid in all settings, and a more detailed consideration of detachment process is required (Whipple et al., 2000; Wilson and Lavé, 2014; Lamb et al., 2015).

We observe a micro-scale (mm – cm) equivalent of step back-wearing (block removal) (Naylor and Stephenson, 2010; Stephenson and Naylor, 2011; Moses, 2014) where erosion is concentrated at small but sharp topographic edges. In these locations detachments can be to the full depth of the edge, but relatively small in planform, akin to the lateral landward retreat of steps, or the erosion of bedrock asperities (Lamb et al., 2015).

The volume-frequency distribution (Figure 5) adheres to the power-law scaling more widely observed in natural and geomorphic phenomena (Malamud et al., 2004). Whilst the scale of investigation is at least five orders of magnitude smaller than commonly considered, the exponent β falls within that previously documented β = 0.4-1.1 for rockfall generally (Santana et al., 2012), and β = 0.71-2.37 for rockfall for the nearby coastal cliffs formed in the same rock types (Rosser et al., 2007; Barlow et al., 2012; Whadcoat, 2017; Williams et al., 2018). Hungr et al. (1999) identified that high β-values are more common for discontinuous as compared to massive rock masses. Here, the rock micro-structure, dominated by laminations in the shale and sandstone, appears to be exploited by marine action and made friable

or can be ‘frittered’ due to exposure at the surface (Moon and Healy, 1994). These properties may be critical in generating such a high exponent, indicative of the dominance of smaller detachments (Malamud et al., 2004).

A rollover, indicated by a reduction in small detachment volume (< 1.12×10^{-8} m^3) frequency compared to that predicted by the power-law model, is evident in our dataset (Figure 5) and can be explained by either censoring due to the spatial resolution of the monitoring method, by superimposition or coalescence of smaller detachment scars within single monitoring epochs, or as a function of a limit on detachment size imposed by either the erosion processes or rock (micro) structure (Malamud et al., 2004). Dussauge-Peisser et al. (2002), in a study of rockfall, suggested that the smallest detachment geometry may depend on the condition of rock surface, as affected by the air temperature and the freeze/thaw cycles. Conversely, the characteristics of medium to large events are more dependent on the rock properties, such as the discrete fracture network and the intact rock strength. In this instance, the physical, chemical and biological weathering within the intertidal environment may contribute to promoting the release and erosion of the smallest particles which have volumes comparable to the grain size (10^{-4} m). Notably, organisms (algae and animals) can play a pivotal role in enhancing (Torunski, 1979; Andrews and Williams 2000; Naylor et al., 2012) or impeding (Coombes et al., 2017) bedrock erosion at the (sub) mm scale, as conceptually shown in Figure 11. However, our data do not allow any firm conclusions to be drawn about the importance of biological activity in directly causing and/or moderating erosion. Larger-scale rock properties (10^{-3} – 10^{-1} m), in particular in this case the laminations, flaking or jointing, likely control the geometry and location of the larger detachments.

The complex shape of the volume-frequency relationship implies that our observed detachments are likely the cumulative result of several superimposed populations that result from discrete processes (Figure 5). We draw this conclusion from the combination of the sharp inflection in the slope of the distribution at a detachment size equivalent to a single shale flake (equivalent to the volume of a 0.011 m cube) and the high scaling exponent β for volume > 1.26×10^{-6} m^3. This suggests that platelet detachment is far more frequent, and in sum far more an effective contributor to erosion of the shore platform, than discrete block removal. The subtle peaks at smaller detachment volumes may also have a physical explanation rather than being purely noise in the data given the high sample numbers in our inventory, and may reflect different mechanisms dominating at different scales. However, given dominance of small detachments in the overall distribution, and the concentration of their geometry at dimensions equal to or small multiples of our monitoring resolution, this remains challenging to establish with certainty (Figure 5). When upscaling, the understanding of the dominant processes on erosion patterns and how this is temporally manifest is more credible than generalised erosion rates, and can feed into coastal evolution models to consider how shore platform change may alter wider hydrodynamic forcing and associated feedbacks on erosion (Kline et al., 2014; Limber et al., 2014; Hurst et al., 2016; Matsumoto et al., 2016). We hypothesise that a longer monitoring period would result in the detection of low-frequency, larger detachments, such that volume-frequency distribution maintains the observed power-law trend.

The dominance of detachments located closer to the seaward edge for slab-like shapes (Figure 6) may indicate the shear of laminations at the sandstone sites as a mechanism of erosion. Conversely, closer to the cliff, weathering

(wetting/drying) likely causes more intense cracking which predefines blocks to release. Overall, the characteristic shape of most detachments (*very bladed* and *very platy*) reaffirms the platelet form of most detachments, which again supports the mechanisms described above (Figure 6).

Controls on the spatial distribution of erosion

The results of our data analysis suggest that, while local erosion is in part a function of position on shore platform which defines the level of exposure to assailing hydraulic action and wetting, the nature of erosion itself, as represented by the size distribution of detachments, depends on the local micro-relief. Topographic edges and exposed free-to-release platelets provide the surface and micro-structural conditions necessary for enabling detachments to be released.

The observed erosion rate has been shown to be a function of the distances from the foreshore seaward limit and tidal duration. It seems probable that the positive relationship with the distance from the seaward edge reflects the more favourable hydraulic conditions at the cliff toe (usually characterised also by higher values of elevation, slope and roughness), which drive higher rates of erosion in this location, as observed elsewhere (Robinson, 1977; Stephenson and Kirk, 1998; Foote et al., 2006; Moses and Robinson, 2011). The relationships support the theoretical (Flemming, 1965; Sunamura, 1992) and the exploratory numerical (Kline et al., 2014; Matsumoto et al., 2016) models of coastal cross-section wave energy dissipation and erosive action. Our findings also agree with the influence of observations of wave attenuation across micro-tidal platforms, where the greatest wave heights occur close to the cliff toe (Stephenson et al., 2018). The observed positive correlation between erosion rates and tidal duration suggests that more

erosion happens due to hydraulic force or wedging at locations over which the tide cycles more frequently (Figure 11).

The relationship between site roughness and erosion parameters, including the mean volume and the exponent β (Table 4; Figure 9), suggest that micro-topography has a profound influence on the size of eroded detachments, with a more diverse range of detachment sizes observed at more irregular surfaces. The micro-topography of the platform is also intimately linked to the rock micro-structure, where shale platelets create higher micro-relief than sandstone, which has near-horizontal micro-layers without protruding rock fragments exposed to release. The lack of relationship between surface roughness and erosion rates agrees with the observations of Poate et al. (2018).

Our regression analysis allows a reasonable estimation of local erosion rate across the shore platform based on locational, topographic and tidal controls (Table 4). The model preforms well when validated using the test set (Figure 10). Site 12 is the only location which shows a significant (at 95% confidence interval) discrepancy between the predicted and observed erosion values. The site is located directly behind a boulder (1.5 × 1.2 × 0.8 m), which may influence the local hydrodynamics. The boulder may afford this section some protection from assailing waves, which implies that platforms with more frequent boulder cover, may experience significant local variability in down-wearing rates (Moses, 2014; Wilson and Lavé, 2014). Therefore, we treat the site as an outlier relative to the other sites.

We observe an increase in erosion that appears to be a function of proximity to the cliff, and local gradient, which may reflect difference in turbulence when submerged and flow due to platform drainage as the tide recedes (Robinson, 1977). We consider these spatial patterns to be, in part, a function of current foreshore

morphology and its relationship with prevailing relative sea-level and tidal conditions; should rates relative sea-level and/or platform morphology change, so too will the locations at which the nature and intensity of erosion occur. This should be carefully considered when modelling long-term erosion rates (Trenhaile, 1983; 2000; Walkden and Hall, 2005; Kline et al., 2014; Limber et al., 2014).

Controls on the temporal distribution of erosion

We observe an apparent increase in erosion during summer months, which concurs with the observations of Robinson (1977), Mottershead (1989) and Stephenson and Kirk (1998; 2001). Detached rock fragments are more diverse size-wise and generally larger in the summer months. We ascribe this to the role of expansion and contraction on platelet detachment intensified in summer months when maximum temperatures increase the probability of the thermal fatigue, thermal shock and expansion of salts which each can cause rock breakdown (Coombes, 2014).

Robinson (1977) observed faster erosion of the planar, seaward part of the foreshore in summer and of the ramp in winter. He ascribed this difference to the dominance of weathering and abrasion for respective sections of the foreshore throughout the year. Our sites proximal to the cliff toe also displayed slightly higher erosion rates in summer months. The availability of abrasive sediment is more important than platform morphology (i.e. slope) and cross-shore location in determining whether weathering or abrasion dominates erosion.

Notably, our monitoring campaign lasted one year only, and so longer monitoring period is needed to provide more meaningful information about temporal (intra- and inter-annual) distribution of erosion.

Wider implications

The spatial and temporal distribution of erosion across the platform and through the year of monitoring provides new insight into the magnitude-frequency distribution of shore platform erosion at the sub-metre scale (Figure 8). The differences in the magnitude of erosion and the area and volume of individual detachments across the two rock types suggests that: 1) larger detachments are more likely in shale; 2) the erosion rates vary more as a function of position on the platform than as a function of time of year; and, 3) that whilst individual sites for individual months show variability, there is a general gradient in erosion rate, detachment frequency, and detachment size across the platform. This gradient can be modelled and predicted statistically, and used to model coastal evolution and to assess shore platform exposure ages using cosmogenic isotope concentrations (Choi et al., 2012; Regard et al., 2012; Hurst et al., 2016; 2017). Moreover, the volume-frequency distribution (Figure 5) provides information about detachment occurrence over a larger range of spatial scales than previously, covering volumes from 10^{-9} to 10^{-4} m^3. If the observed relationship holds across all scales, the results can be upscaled to serve as the basis for constraining the probability of detachment occurrence in landscape evolution models (Matsumoto et al., 2016).

Summary

We have presented a method to monitor shore platform bedrock erosion using SfM photogrammetry. We optimised the number of camera positions to be able to resolve 0.001 m vertical change within a 0.5 × 0.5 m plot at 0.001 m pixel resolution. We analysed the nature of erosion on the basis of detachment inventory which

allowed us constrain the mechanisms of shore platform down-wearing and controls on its spatial and temporal variability.

Our key conclusions can be summarised as follows:

1. The down-wearing rate of the Hartle Loup shore platform was 0.528 mm yr^{-1} in 2016 - 2017, but varied between 0.101 and 1.192 mm yr^{-1} between our 15 monitoring sites, and between 0.576 and 0.497 mm yr^{-1} between the periods of April to October and October to April.
2. The volume-frequency and 3D-shape distributions of the detachments suggest that erosion happens predominantly via detachment of platelets.
3. The size distribution shows that the single shale-platelet size is a threshold size above which the detachments are extremely rare (β = 2.534).
4. The magnitude of erosion expressed by the erosion rate and the total eroded volume is a function of the location on the shore platform with more erosion happening closer to the cliff, farther from the seaward edge where elevation and slope are higher.
5. The size distribution of detachments is controlled by the surface micro-topography which, in turn, depends on the rock micro-structure.
6. Faster erosion and larger, more diverse size-wise detachments occur in the Northern Hemisphere summer months.
7. Our high-resolution results can inform numerical models of hard-rock coastal evolution and improve the accuracy of geochronological studies of the cliff retreat using the cosmogenic isotope concentrations in shore platform lithologies. Specifically, we highlight importance of identifying contemporary processes and spatial distribution of erosion.

Supplementary materials

The supplementary document contains the details about: the optimisation of the number of photographs, the GCP and CP location error, UAV surveying and georeferencing, applied size and shape filters, independent validation of the method and estimation of the result uncertainty.

Acknowledgements

We are grateful to ICL Fertilizers UK Ltd for supporting the research. The tidal data was downloaded from the NERC British Oceanographic Data Centre (https://www.bodc.ac.uk/) and the National Tidal and Sea Level Facility (https://www.ntslf.org/) websites. We would like to thank a number of colleagues who helped at various stages of the projects: Marek Ewertowski, Patrice Carbonneau, Emma Vann Jones and Mike Lim provided insightful comments at the early stages of method development; Wayne Stephenson and Sarah Woodroffe provided feedback on the underpinning research; multiple colleagues assisted in the field; and Jack Williams provided the code to create Figure 6. We thank the associate editor and two anonymous reviewers for their helpful and constructive comments. This paper is a contribution to IGCP Project 639: "*Sea-level change from minutes to millennia*".

References

Andrade C, Marques F, Freitas MC, Cardos R, Madureira P. 2002. Shore platform downwearing and cliff retreat in the Portuguese west coast. In Littoral 2002, The Changing Coast. EUROCOAST/EUCC, Pozar-Domac A (ed.): Porto; 423-431.

Andrews C, Williams RBG. 2000. Limpet erosion of chalk shore platforms in Southeast England. Earth Surface Processes and Landforms 25: 1371-1381.

Barlow J, Lim M, Rosser N, Petley D, Brain M, Norman E, Geer M. 2012. Modeling cliff erosion using negative power law scaling of rockfalls. Geomorphology 139-140: 416-424. DOI: 10.1016/j.geomorph.2011.11.006

Benjamin J, Rosser NJ, Brain MJ. In review. Emergent characteristics of 3D rockfall inventories captured over large spatial extents. Journal of Geophysical Research: Earth Surface.

Blanco-Chao R, Pérez-Alberti A, Trenhaile AS, Costa-Casais M, Valcárcel-Díaz M. 2007. Shore platform abrasion in a para-periglacial environment, Galicia, northwestern Spain. Geomorphology 83: 136-151. DOI: 10.1016/j.geomorph.2006.06.028

Choi KH, Seong YB, Jung PM, Lee SY. 2012 Using Cosmogenic 10Be Dating to Unravel the Antiquity of a Rocky Shore Platform on the West Coast of Korea. Journal of Coastal Research 28(3): 641-657. DOI: 10.2112/JCOASTRES-D-11-00087.1

Clauset A, Shalizi CR, Newman MEJ. 2009. Power-law distributions in empirical data. SIAM Review 51(4): 661-703. DOI: 10.1137/070710111

Cook KL. 2017. An evaluation of the effectiveness of low-cost UAVs and structure from motion for geomorphic change detection. Geomorphology 278: 195-208. DOI: 10.1016/j.geomorph.2016.11.009

Coombes MA. 2014. The rock coast of the British Isles: weathering and biogenic processes. Geological Society, London, Memoirs 40: 57-76. DOI: 10.1144/M40.5

Coombes MA, Viles HA, Naylor LA, La Marca EC. 2017. Cool barnacles: Do common biogenic structures enhance or retard rates of deterioration of intertidal rocks and concrete? Science of the Total Environment 580: 1034-1045. DOI: 10.1016/j.scitotenv.2016.12.058

Cullen ND, Bourke MC. 2018. Clast abrasion of a rock shore platform on the Atlantic coast of Ireland. Earth Surface Processes and Landforms. DOI: 10.1002/esp.4421

Cullen ND, Verma AK, Bourke MC. 2018. A comparison of Structure from Motion Photogrammetry and the Traversing Micro Erosion Meter for measuring erosion on rock shore platforms. Earth Surface Dynamics 6: 1023-1039. DOI: 10.5194/esurf-6-1023-2018

Dasgupta R. 2010. Whither shore platforms? Progress in Physical Geography 35(2): 183-209. DOI: 10.1177/0309133310375730

Dickson ME, Ogawa H, Kench PS. 2013. Sea-cliff retreat and shore platform widening: steady-state equilibrium? Earth Surface Processes and Landforms 38: 1046-1048

Dornbusch U, Robinson DA. 2011. Block removal and step backwearing as erosion processes on rock shore platforms: a preliminary case study of the chalk shore platforms of south-east England. Earth Surface Processes and Landforms 36(5): 661-671. DOI: 10.1002/esp.2086

Dornbusch U, Robinson DA, Moses CA, Williams RBG. 2006. Chalk coast erosion and its contribution to the shingle budget in East Sussex. Zeitschrift für Geomorphologie Supplementbände 144: 215-230.

Dussauge-Peisser C, Helmstetter A, Grasso J-R, Hantz D, Desvarreux P, Jeannin M, Giraud A. 2002. Probabilistic approach to rock fall hazard assessment: potential of historical data analysis. Natural Hazards and Earth System Sciences 2: 15-26. DOI: 10.5194/nhess-2-15-2002

Flemming NC. 1965. Form and Relation to Present Sea Level of Pleistocene Marine Erosion Features. The Journal of Geology 73: 799-811.

Foote Y, Plessis E, Robinson DA, Henaff A, Costa S. 2006. Rates and patterns of downwearing of chalk shore platforms of the Channel: comparisons between France and England. Zeitschrift für Geomorphologie Supplementbände 144: 93-115.

Gonçalves JA, Henriques R. 2015. UAV photogrammetry for topographic monitoring of coastal areas. ISPRS Journal of Photogrammetry and Remote Sensing 104: 101-111. DOI: 10.1016/j.isprsjprs.2015.02.009

Grenness MJ, Osborn JE, Tyas MJ. 2005. Stereo-Photogrammetric Mapping of Tooth Replicas Incorporating Texture. The Photogrammetric Record 20: 147-161. DOI: 10.1111/j.1477-9730.2005.00311.x

Guzzetti F, Ardizzone F, Cardinali M, Rossi M, Valigi D. 2009. Landslide volumes and landslide mobilization rates in Umbria, central Italy. Earth and Planetary Science Letters 279(3): 222-229. DOI: 10.1016/j.epsl.2009.01.005

Hungr O, Evans S, Hazzard J. 1999. Magnitude and frequency of rock falls and rock slides along the main transportation corridors of southwestern British Columbia. Canadian Geotechnical Journal 36: 224-238.

Hurst MD, Rood DH, Ellis MA, Anderson RS, Dornbusch U. 2016. Recent acceleration in coastal cliff retreat rates on the south coast of Great Britain. Proceedings of the National Academy of Sciences of the United States of America 113(47): 13336-13341. DOI: 10.1073/pnas.1613044113

Hurst MD, Rood DH, Ellis MA. 2017. Controls on the distribution of cosmogenic 10Be across shore platforms. Earth Surface Dynamics Discussions 5: 67-84. DOI: 10.5194/esurf-2016-42

James MR, Robson S, Smith MW. 2017. 3-D uncertainty-based topographic change detection with structure-from-motion photogrammetry: precision maps for ground

control and directly georeferenced surveys. Earth Surface Processes and Landforms 42(12): 1769-1788. DOI: 10.1002/esp.4125

Kalenchuk KS, Diederichs MS, McKinnon S. 2006. Characterizing block geometry in jointed rockmasses. International Journal of Rock Mechanics and Mining Sciences 43: 1212-1225. DOI: 10.1016/j.ijrmms.2006.04.004

Kirk RM. 1977. Rates and forms of erosion on intertidal platforms at Kaikoura Peninsula, South Island, New Zealand. New Zealand Journal of Geology and Geophysics 20: 571–613.

Kline SW, Adams PN, Limber PW. 2014. The unsteady nature of sea cliff retreat due to mechanical abrasion, failure and comminution feedbacks. Geomorphology 219: 53-67. DOI: 10.1016/j.geomorph.2014.03.037

Lamb MP, Finnegan NJ, Scheingross JS, Sklar LS. 2015. New insights into the mechanics of fluvial bedrock erosion through flume experiments and theory. Geomorphology 244: 33-55. DOI: 10.1016/j.geomorph.2015.03.003

Larsen IJ, Montgomery DR, Korup O. 2010. Landslide erosion controlled by hillslope material. Nature Geoscience 3(4): 247-251. DOI: 10.1038/NGEO776

Limber PW, Murray AB, Adams PN, Goldstein EB. 2014. Unraveling the dynamics that scale cross-shore headland relief on rocky coastlines: 1. Model development. Journal of Geophysical Research: Earth Surface 119. DOI: 10.1002/2013JF002950

Malamud BD, Turcotte DL, Guzzetti F, Reichenbach P. 2004. Landslide inventories and their statistical properties. Earth Surface Processes and Landforms 29: 687-711. DOI: 10.1002/esp.1064

Marteau B, Vericat D, Gibbins C, Batalla RJ, Green DR. 2017. Application of Structure-from-Motion photogrammetry to river restoration. Earth Surface Processes and Landforms 42: 503-515. DOI: 10.1002/esp.4086

Matsumoto H, Dickson ME, Kench PS. 2016. An exploratory numerical model of rocky shore profile evolution. Geomorphology 268: 98-109. DOI: 10.1016/j.geomorph.2016.05.017

Mayaud JR, Viles HA, Coombes MA. 2014. Exploring the influence of biofilm on short-term expansion and contraction of supratidal rock: an example from the Mediterranean. Earth Surface Processes and Landforms 39: 1404-1412. DOI: 10.1002/esp.3602

Moon VG, Healy T. 1994. Mechanisms of coastal cliff retreat and hazard zone delineation in soft flysch deposits. Journal of Coastal Research 10(3): 663-680.

Moses C, Robinson D. 2011. Chalk coast dynamics: Implications for understanding rock coast evolution. Earth-Science Reviews 109: 63-73. DOI: 10.1016/j.earscirev.2011.08.003

Moses CA. 2014. Chapter 4 The rock coast of the British Isles: shore platforms. Geological Society, London, Memoirs 40: 39-56. DOI: 10.1144/M40.4

Mottershead DN. 1989. Rates and patterns of bedrock denudation by coastal salt spray weathering: a seven-year record. Earth Surface Processes and Landforms 14: 383-398.

Moura D, Gabriel S, Ramos-Pereira A, Neves M, Trindade J, Viegas J, Veiga-Pires C, Ferreira Ó, Matias A, Jacob J, Boski T, Santana P. 2011. Downwearing rates on shore platforms of different calcareous lithotypes. Marine Geology 286: 112-116.

Naylor LA, Coombes MA, Viles HA. 2012. Reconceptualising the role of organisms in the erosion of rock coasts: a new model. Geomorphology 157–158: 17-30. DOI: 10.1016/j.geomorph.2011.07.015

Naylor LA, Stephenson WJ. 2010. On the role of discontinuities in mediating shore platform erosion. Geomorphology 114: 89-100. DOI: 10.1016/j.geomorph.2008.12.024

Nitsche M, Turowski JM, Badoux A, Rickenmann D, Kohoutek TK, Pauli M, Kirchner JW. 2013. Range imaging: a new method for high-resolution topographic measurements in small- and medium-scale field sites. Earth Surface Processes and Landforms 38: 810-825. DOI: 10.1002/esp.3322

Ogawa H, Dickson ME, Kench PS. 2016. Generalised observations of wave characteristics on near-horizontal shore platforms: Synthesis of six case studies from the North Island, New Zealand. New Zealand Geographer 72(2): 107-121. DOI: 10.1111/nzg.12121

Parker RN, Hancox GT, Petley DN, Massey CI, Densmore AL, Rosser NJ. 2015. Spatial distributions of earthquake-induced landslides and hillslope preconditioning in northwest South Island, New Zealand. Earth Surface Dynamics Discussion 3: 1-52. DOI: 10.5194/esurfd-3-1-2015

Poate T, Masselink G, Austin M, Dickson M, McCall R. 2018. The role of bed roughness in wave transformation across sloping rock shore platforms. Journal of Geophysical Research: Earth Surface 123: 97-123. DOI: 10.1002/2017JF004277

Porter NJ, Trenhaile AS. 2007. Short-term rock surface expansion and contraction in the intertidal zone. Earth Surface Processes and Landforms 32: 1379-1397. DOI: 10.1002/esp.1479

Rawson PF, Wright JK. 2000. The Yorkshire coast (3rd ed). Geologists' Association Guide 34. The Geologists' Association.

Regard V, Dewez T, Bourlès DL, Anderson RS, Duperret A, Costa S, Leanni L, Lasseur E, Pedoja K, Maillet GM. 2012. Late Holocene seacliff retreat recorded by

10Be profiles across a coastal platform: Theory and example from the English Channel. Quaternary Geochronology 11: 87-97. DOI: 10.1016/j.quageo.2012.02.027

Robinson LA. 1976. The micro-erosion meter technique in a littoral environment. Marine Geology 22: M51-M58.

Robinson LA. 1977. Erosive processes on the shore platform of northeast Yorkshire, England. Marine Geology 23: 339-361.

Rock G, Ries JB, Udelhoven T. 2011. Sensitivity analysis of UAV-photogrammetry for creating Digital Elevation Models (DEM). In Proceedings of Conference on Unmanned Aerial Vehicle in Geomatics. Zurich, Switzerland.

Rosser NJ, Lim M, Petley D, Dunning S, Allison R. 2007. Patterns of precursory rockfall prior to slope failure. Journal of Geophysical Research 112. DOI: 10.1029/2006JF000642

Rosser NJ, Brain MJ, Petley DN, Lim M, Norman EC. 2013. Coastline retreat via progressive failure of rocky coastal cliffs. Geology 41(8): 939-942. DOI: 10.1130/G34371.1

Santana D, Corominas J, Mavrouli O, Garcia-Sellés D. 2012. Magnitude-frequency relation for rockfall scars using a Terrestrial Laser Scanner. Engineering Geology 145: 50-64. DOI: 10.1016/j.enggeo.2012.07.001

Smith MW. 2015. Direct acquisition of elevation data: Terrestrial Laser Scanning, In Geomorphological Techniques, Clarke L (ed.). British Society for Geomorphology: London.

Sneed ED, Folk RL. 1958. Pebbles in the Lower Colorado River, Texas a Study in Particle Morphogenesis. The Journal of Geology 66: 114-150.

Stephenson WJ. 2000. Shore platforms: a neglected coastal feature? Progress in Physical Geography 24: 311-327. DOI: 10.1177/030913330002400301

Stephenson WJ, Finlayson BL. 2009. Measuring erosion with the micro-erosion meter—Contributions to understanding landform evolution. Earth-Science Reviews 95: 53-62. DOI: 10.1016/j.earscirev.2009.03.006

Stephenson WJ, Kirk RM. 1998. Rates and patterns of erosion on inter-tidal shore platforms, Kaikoura Peninsula, South Island, New Zealand. Earth Surface Processes and Landforms 23: 1071-1085. DOI: 10.1002/(SICI)1096-9837(199812)23:12<1071::AID-ESP922>3.0.CO;2-U

Stephenson WJ, Kirk RM. 2001. Surface swelling of coastal bedrock on inter-tidal shore platforms, Kaikoura Peninsula, South Island, New Zealand. Geomorphology 41: 5-21. DOI: 10.1016/S0169-555X(01)00100-3

Stephenson WJ, Naylor LA. 2011. Geological controls on boulder production in a rock coast setting: Insights from South Wales, UK. Marine Geology 283: 12-24. DOI: 10.1016/j.margeo.2010.07.001

Stephenson WJ, Naylor LA, Smith H, Chen B, Brayne RP. 2018. Wave transformation across a macrotidal shore platform under low to moderate energy conditions. Earth Surface Processes and Landforms 43: 298-311. DOI: 10.1002/esp.4245

Sunamura T. 1992. Geomorphology of Rocky Coasts. John Wiley & Sons Ltd: Chichester.

Swantesson JOH, Gómez-Pujol L, Cruslock EM, Fornós JJ, Balaguer P. 2006. Processes and patterns of erosion and downwearing on micro-tidal rock coasts in Sweden and western Mediterranean. Zeitschrift für Geomorphologie Supplementbände 144: 137-160.

Swirad ZM, Rosser NJ, Brain MJ, Vann Jones EC. 2016. What controls the geometry of rocky coasts at the local scale? Journal of Coastal Research SI75: 612-616: DOI: 10.2112/SI75-123.1

Taylor AJ. 2003. Change and processes of change on shore platforms. PhD thesis: University of Canterbury, Christchurch, New Zealand.

Torunski H. 1979. Biological erosion and its significance for the morphogenesis of limestone coasts and for nearshore sedimentation. Senckenbergiana Maritima 11: 193-265.

Trenhaile AS. 1983. The width of shore platforms; a theoretical approach. Geografiska Annaler. Series A, Physical Geography 65: 147-158. DOI: 10.2307/520728

Trenhaile AS. 2000. Modeling the development of wave-cut shore platforms. Marine Geology 166: 163-178. DOI: 10.1016/S0025-3227(00)00013-X

Turowski JM, Cook KL. 2017. Field techniques for measuring bedrock erosion and denudation. Earth Surface Processes and Landforms 42: 109-127. DOI: 10.1002/esp.4007

Viles H, Goudie A, Grab S, Lalley J. 2011. The use of the Schmidt Hammer and Equotip for rock hardness assessment in geomorphology and heritage science: a comparative analysis Earth Surface Processes and Landforms 36: 320-333. DOI: 10.1002/esp.2040

Wackrow R, Chandler JH. 2008. A convergent image configuration for DEM extraction that minimises the systematic effects caused by an inaccurate lens model. The Photogrammetric Record 23: 6-18. DOI: 10.1111/j.1477-9730.2008.00467.x

Wackrow R, Chandler JH, Bryan P. 2007. Geometric consistency and stability of consumer-grade digital cameras for accurate spatial measurement. The Photogrammetric Record 22: 121-134. DOI: 10.1111/j.1477-9730.2007.00436.x

Walkden MJA, Hall JW. 2005. A predictive Mesoscale model of the erosion and profile development of soft rock shores. Coastal Engineering 52: 535-563. DOI: 10.1016/j.coastaleng.2005.02.005

Westoby MJ, Brasington J, Glasser NF, Hambrey MJ, Reynolds JM. 2012. "Structure-from-Motion" photogrammetry: A low-cost, effective tool for geoscience applications. Geomorphology 179: 300-314. DOI: 10.1016/j.geomorph.2012.08.021

Whadcoat SK. 2017. Numerical modelling of rockfall evolution in hard rock slopes. PhD thesis: Durham University, Durham.

Whipple KX, Hancock GS, Anderson RS. 2000. River incision into bedrock: Mechanics and relative efficacy of plucking, abrasion, and cavitation. GSA Bulletin 112(3): 490-503.

Williams JG, Rosser NJ, Hardy RJ, Brain MJ, Afana AA. 2018. Optimising 4-D surface change detection: an approach for capturing rockfall magnitude-frequency. Earth Surface Dynamics 6: 101-119. DOI: 10.5194/esurf-6-101-2018

Wilson A, Lavé J. 2014. Convergent evolution of abrading flow obstacles: Insights from analogue modelling of fluvial bedrock abrasion by coarse bedload. Geomorphology 2018: 207-224. DOI: 10.1016/j.geomorph.2013.11.024

Table 1. General characteristics of the monitoring sites. See Table 2 for calculation of the variable values.

Site	Distance from the cliff, *Cli* (m)	Distance from the seaward edge, *Sea* (m)	Elevation, *Ele* (m AOD)	Slope, *Slo* (°)	Rough-ness, *Rou* (°)	Tidal duration, *Tid* (%)	Inundation frequency, *Inu* (%)	Rock type	Style of relief	Curvature, *Cur* ($\times 10^{-6}$)	Site roughness, *SRou* (°)	Elevation range, *EleR* (m)	Number of joints, *JNo*	Length of joints, *JLe* (m)
1	42.9	118.5	1.38	29.71	8.33	2.72	29.18	Sandstone	Stepped (15 cm)	-7.5	14.27	0.20	3	0.85
2	60.4	135.6	0.22	8.28	3.31	2.07	54.39	Sandstone	Planar	-0.5	10.25	0.07	11	1.56
3	12.0	153.7	1.25	14.41	5.37	2.67	32.00	Shale	Stepped (3 cm)	-1.7	13.31	0.14	0	0
4	26.3	175.7	0.21	3.43	3.39	2.09	54.79	Shale	Planar	-0.1	11.06	0.06	2	0.98
5	76.3	84.2	-0.52	8.08	2.90	2.57	72.87	Sandstone	Stepped (1 cm)	0.6	8.04	0.09	1	0.20
6	106.5	86.9	-0.70	1.38	2.47	2.56	75.44	Shale	Planar	-1.0	10.93	0.07	9	2.03
7	149.6	51.8	-0.44	3.66	2.33	2.55	70.32	Sandstone	Planar	-2.5	9.95	0.05	1	0.48
8	108.8	86.7	-0.49	2.66	1.76	2.55	70.32	Shale	Planar	1.4	9.65	0.04	6	1.63
9	61.6	143.5	-0.33	17.46	10.41	2.43	67.89	Shale	Sloping (15°)	-0.5	15.55	0.18	21	4.57
10	30.7	165.2	0.24	7.87	11.65	2.07	54.39	Shale	Sloping (15°)	2.3	13.87	0.14	8	1.21
11	18.6	177.5	0.75	5.19	7.53	2.16	43.89	Shale	Stepped (6 cm)	4.4	13.81	0.16	4	0.85
12	23.6	184.7	1.09	2.53	17.01	2.35	36.84	Shale	Stepped (2 cm)	-2.5	14.87	0.17	2	0.58
13	61.9	117.1	-0.58	2.30	2.63	2.57	72.87	Sandstone	Planar	-3.3	11.27	0.06	3	1.28
14	15.6	180.6	0.88	5.02	3.49	2.15	41.74	Shale	Planar	-0.4	8.26	0.03	9	2.98
15	33.2	178.5	0.21	2.86	3.26	2.07	54.39	Shale	Planar	0.1	7.66	0.04	0	0

Table 2. Summary of the locational, topographic, tidal, structural and erosional variables used to characterise the monitoring sites in this study.

Variable	Abbreviation	Calculation	Unit
Independent variables at the macro-scale based on the LiDAR dataset (0.1 m resolution):			
Distance from the cliff	*Cli*	The distance between the site and the cliff/platform junction mapped on the basis of the slope map; measured with the ArcMap *Near* tool	m
Distance from the seaward edge	*Sea*	The distance between the site and the seaward edge of the shore platform mapped on the basis of the slope map, GoogleEarth ortho-photomaps and the historical maps; measured with the ArcMap *Near* tool	m
Elevation	*Ele*	The DEM values obtained for the centre of the site using the ArcMap *Extract Values to Points* tool	m AOD
Slope	*Slo*	The slope map values obtained for the centre of the site using the ArcMap *Extract Values to Points* tool	°
Roughness	*Rou*	The roughness map values obtained for the centre of the site using the ArcMap *Extract Values to Points* tool; the roughness was calculated as the standard deviation of slope for 17 × 17 cells square	°
Tidal duration	*Tid*	The fraction of time when the sea level is at a 0.1 m elevation range which encompasses elevation of the site; calculated for the Whitby tide gauge from 2006-2010 hourly data from the NERC British Oceanographic Data Centre (https://www.bodc.ac.uk/)	%
Inundation frequency	*Inu*	The fraction of time when the site remains under water; calculated for the Whitby tide gauge from 2006-2010 hourly data from the NERC British Oceanographic Data Centre (https://www.bodc.ac.uk/)	%
Independent variables at the micro-scale based on the SfM dataset (0.001 m resolution):			
Curvature	*Cur*	The cumulative effect of the profile and surface shape on surface flow; calculated as a mean value of a curvature raster created using the ArcMap *Curvature* tool	n/a
Site roughness	*SRou*	Standard deviation of the slope map	°
Elevation range	*EleR*	Maximum-minimum value of the DEM	m
Number of joints	*JNo*	The number of polylines representing joints manually digitised based on the ortho-photographs	n/a
Length of joints	*JLe*	The total length of polylines representing joints manually digitised based on the ortho-photographs	m

Erosion variables:			
Total area	*Area*	The total number of DoD pixels identified as detached at any time multiplied by the pixel size	m^2
Total volume	*Vol*	The sum of volumes of all detachments	m^3
Mean volume	*Mean*	The mean volume of all detachments	m^3
Standard deviation of volumes	*Std*	Standard deviation of the volumes of all detachments	m^3
Erosion rate	*Ero*	1,000 × *Vol* (m^3) / 0.25 m^2 / 1.01 yr	mm yr^{-1}
Exponent *β*	*β*	The power-law exponent of the volume-frequency distribution	n/a

Table 3. Erosion characteristics of the monitoring sites. The largest values are in bold. See Table 2 for calculation of the variable values.

Site	Total area, *Area* (m^2)	Total volume, *Vol* ($\times 10^{-4}$ m^3)	Erosion rate, *Ero* (mm yr^{-1})	Mean volume, *Mean* ($\times 10^{-7}$ m^3)	Standard deviation of volumes, *Std* ($\times 10^{-7}$ m^3)	Exponent β
1	0.043	0.98	0.387	0.56	1.15	0.555
2	0.020	035	0.140	0.34	0.60	0. 885
3	**0.098**	**3.01**	**1.192**	1.07	3.54	0.697
4	0.093	2.42	0.958	0.84	2.30	0.589
5	0.015	0.26	0.101	0.46	1.14	0.738
6	0.042	0.93	0.368	0.74	2.60	0.682
7	0.044	0.79	0.312	0.50	1.24	0.785
8	0.037	0.63	0.247	0.46	1.16	0.804
9	0.078	1.94	0.770	0.90	2.33	0.592
10	0.067	2.23	0.881	**1.14**	**4.52**	0.582
11	0.083	2.30	0.911	0.97	4.07	0.746
12	0.024	0.55	0.218	0.56	2.31	0.809
13	0.026	0.43	0.169	0.64	1.85	0.765
14	0.095	2.10	0.831	0.47	1.48	0.901
15	0.058	1.12	0.444	0.39	0.91	**0.942**

Table 4. The best-fit numerical models of the erosion variables. See Table 2 for abbreviation meaning and calculation of the variable values.

Erosion variable	Equation	R^2	*p*-value
Erosion rate (mm yr^{-1})	$Ero = -2.01 + 0.01\,Sea + 0.60\,Tid$	0.648	0.004
Mean volume (m^3)	$Mean = (-215.20 + 105.00\,SRou - 19.88\,Slo - 2.03\,Cli) \times 10^{-10}$	0.734	0.003
Exponent β	$\beta = 1.10 - 33.66 \times 10^{-3}\,SRou$	0.457	0.009

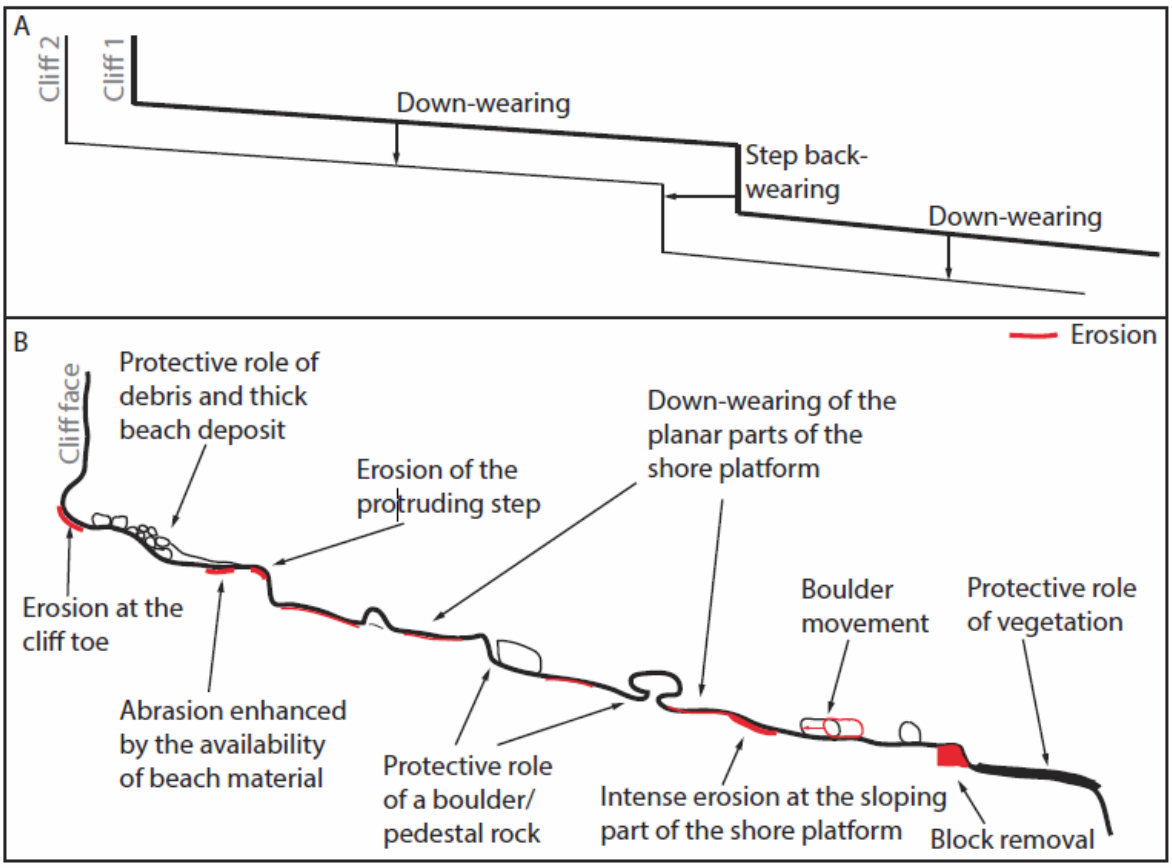

Figure 1. Conceptual summaries of shore platform erosion: A) idealised model of erosion used in many modelling studies of coastal erosion; B) the range of erosional processes and controlling factors reported in the wider literature.

Figure 2. Field evidence of erosion on the Hartle Loup shore platform: A) a step with detached boulder; B) widened and deepened joints; C) fresh exposure of the shale surface showing platelet detachment; D) fresh exposure of the sandstone surface showing micro-layer detachment.

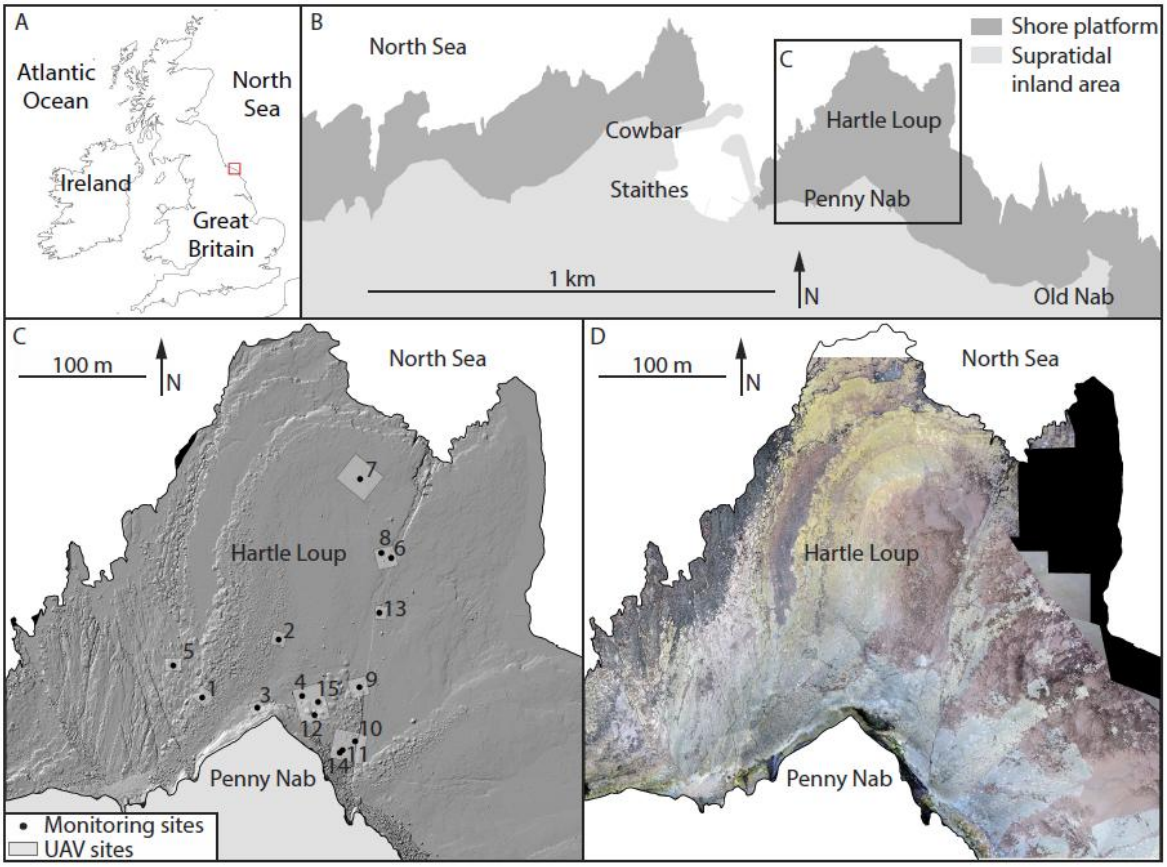

Figure 3. Study area: A) location of North Yorkshire on British Isles (red box); B) shore platform extent in the Staithes area; C) location of the SfM monitoring sites and the UAV sites used for georeferencing the SfM data (Supplementary Material) on the Hartle Loup shore platform overlaid on the LiDAR hillshade; D) LiDAR ortho-photomap mosaic of the Hartle Loup shore platform.

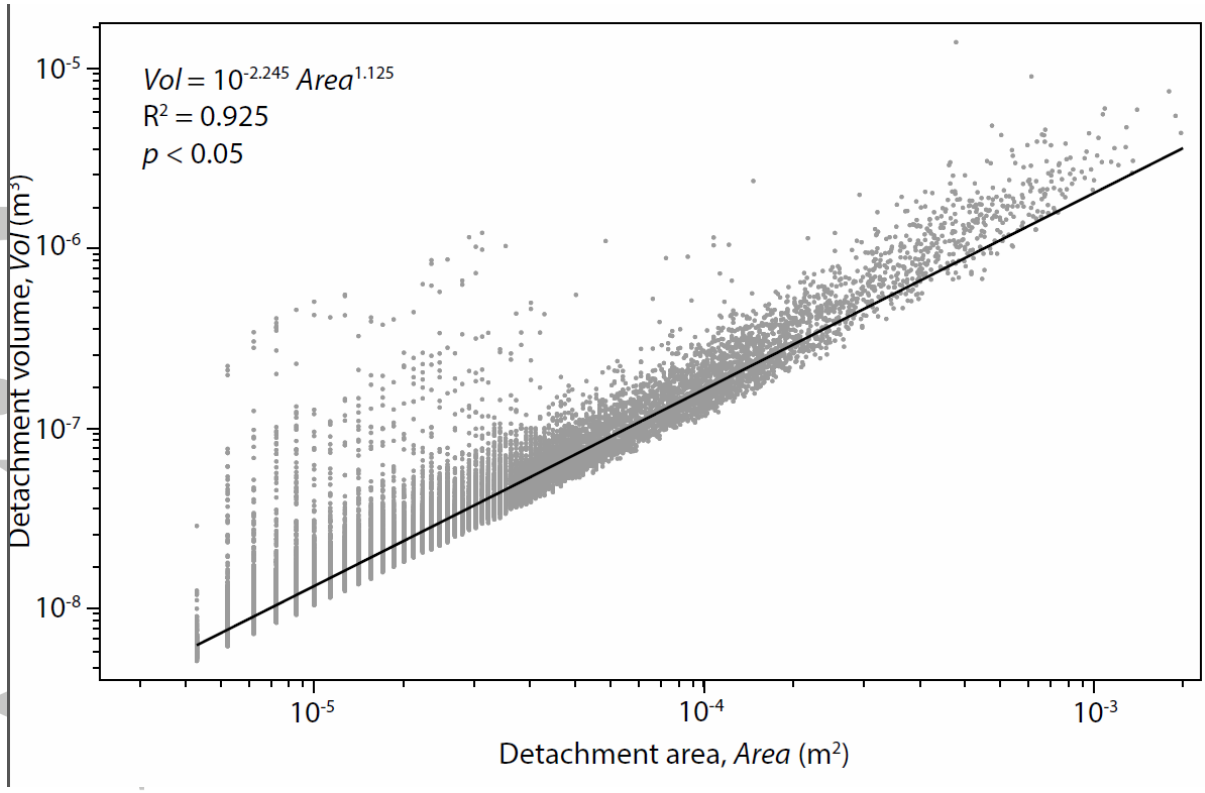

Figure 4. Relationship between detachment area, *Area* (m^2) and detachment volume, *Vol* (m^3) across the full inventory on a log-log non-cumulative plot. Grey points represent single detachments. The black line is the fitted power-law trendline.

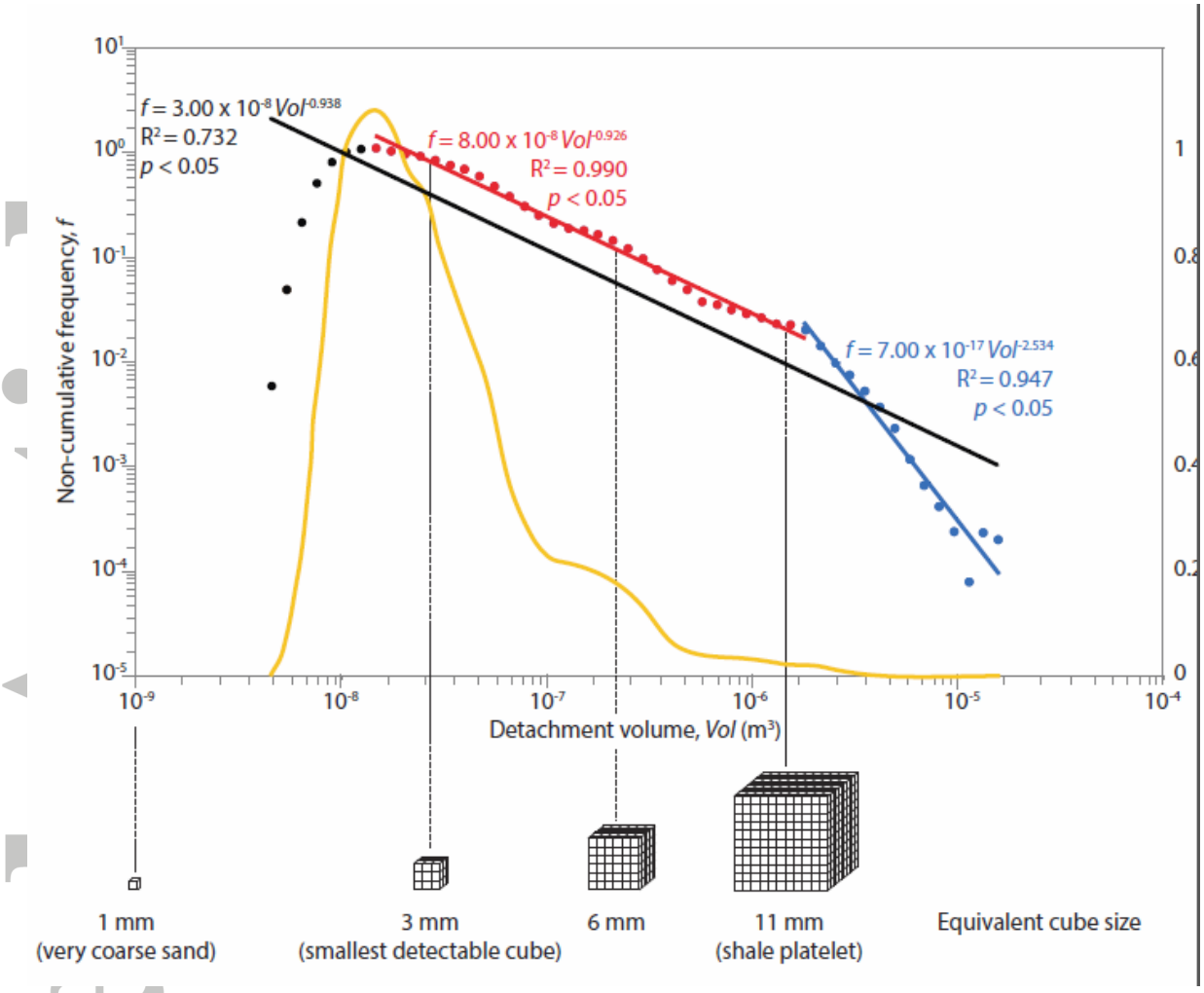

Figure 5. Volume-frequency distribution across the full inventory obtained using SfM methods. Scatter plot (left-hand vertical axis) represents the volume-frequency kernel density distribution curve with the power-law trendline (black line) on a log-log scale plot. Additional trendlines are fitted for two sections of volume spectrum (red for *Vol* 1.12×10^{-8} – 1.26×10^{-6} m^3; blue for *Vol* > 1.26×10^{-6} m^3) excluding the roll-over at the lowest spectrum of *Vol* (black data points). The yellow line is the kernel density estimate (normal kernel, half width = 0.08 $\log_{10}(m^3)$; right-hand vertical axis) of the individual detachment volumes for the full inventory. Idealised shapes indicate the equivalent cube sizes for specific volumes, with indicative relative sizes compared to the possible erosion features.

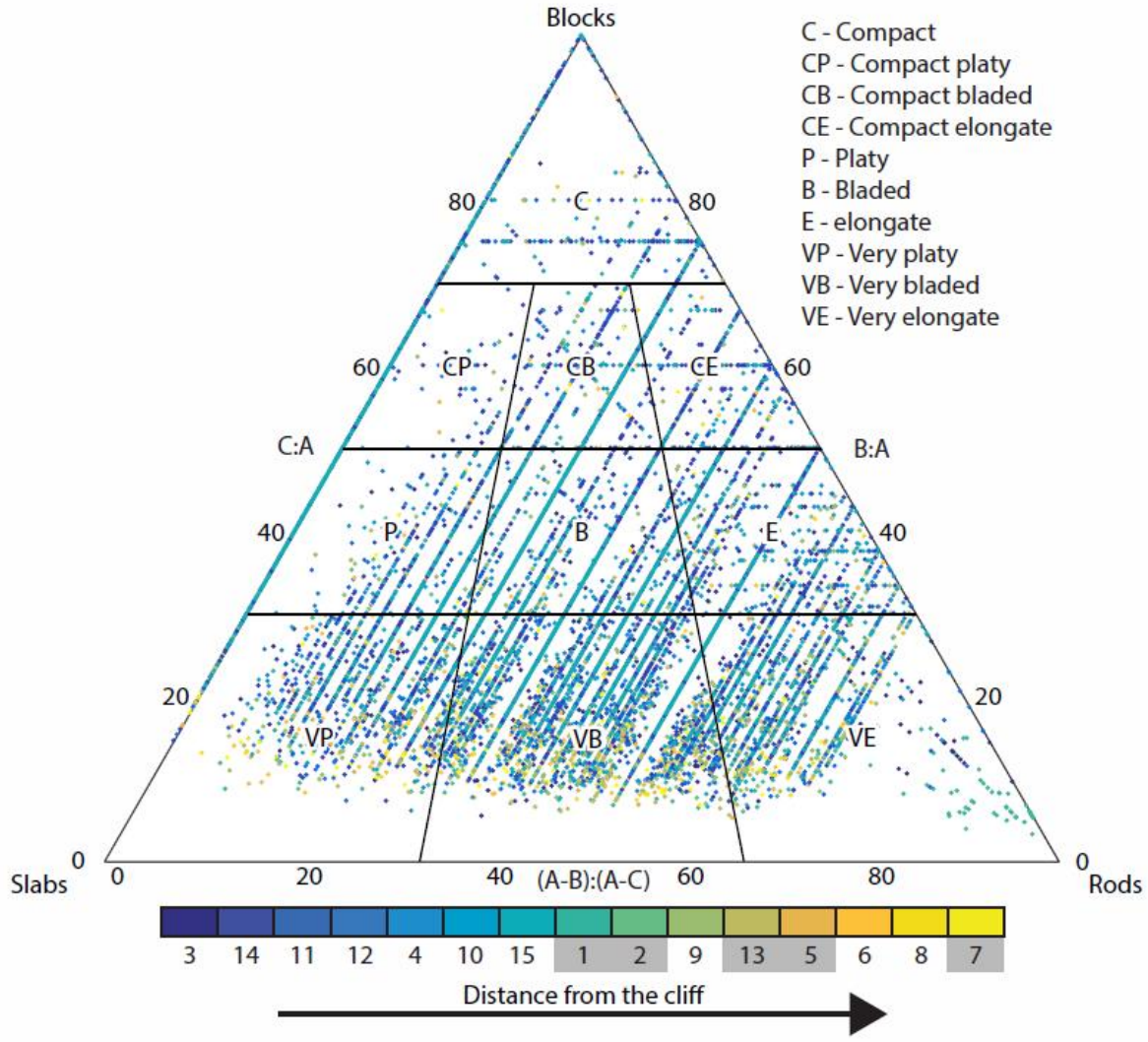

Figure 6. Shapes of detached material coloured by monitoring site, ordered by the distance from the cliff. Block axes: A – long, B – medium, C – short. Sandstone sites are indicated by grey boxes in the lowermost scale; the remaining sites are located on shale sections of the platform.

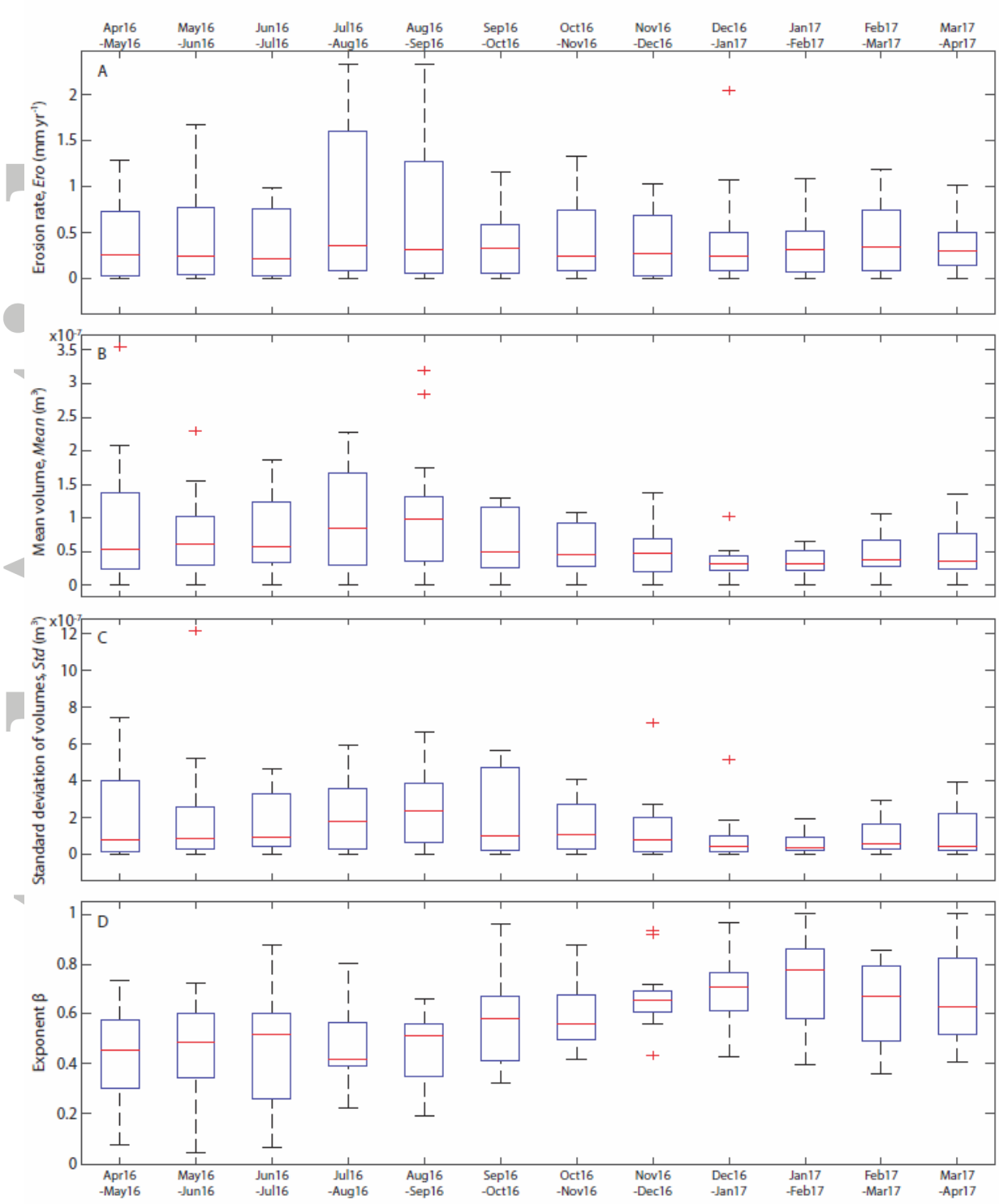

Figure 7. Monthly distribution of the erosion variables as mean values per month: A) Erosion rate, *Ero* (mm yr^{-1}); B) Mean volume, *Mean* (m^3); C) Standard deviation of volumes, *Std* (m^3); D) Exponent *β*. Boxplots contain following information: median (red line), 25-75% interquartile range (blue box), 9-91% quantiles (black lines) and

outliers defined as events greater than *q3 + w (q3 - q1)* or less than *q1 - w (q3 - q1)*, where w is the maximum whisker length, i.e. ± 2.7 standard deviation, and *q1* and *q3* are the 25^{th} and 75^{th} percentiles of the sample data, respectively (red plus symbols).

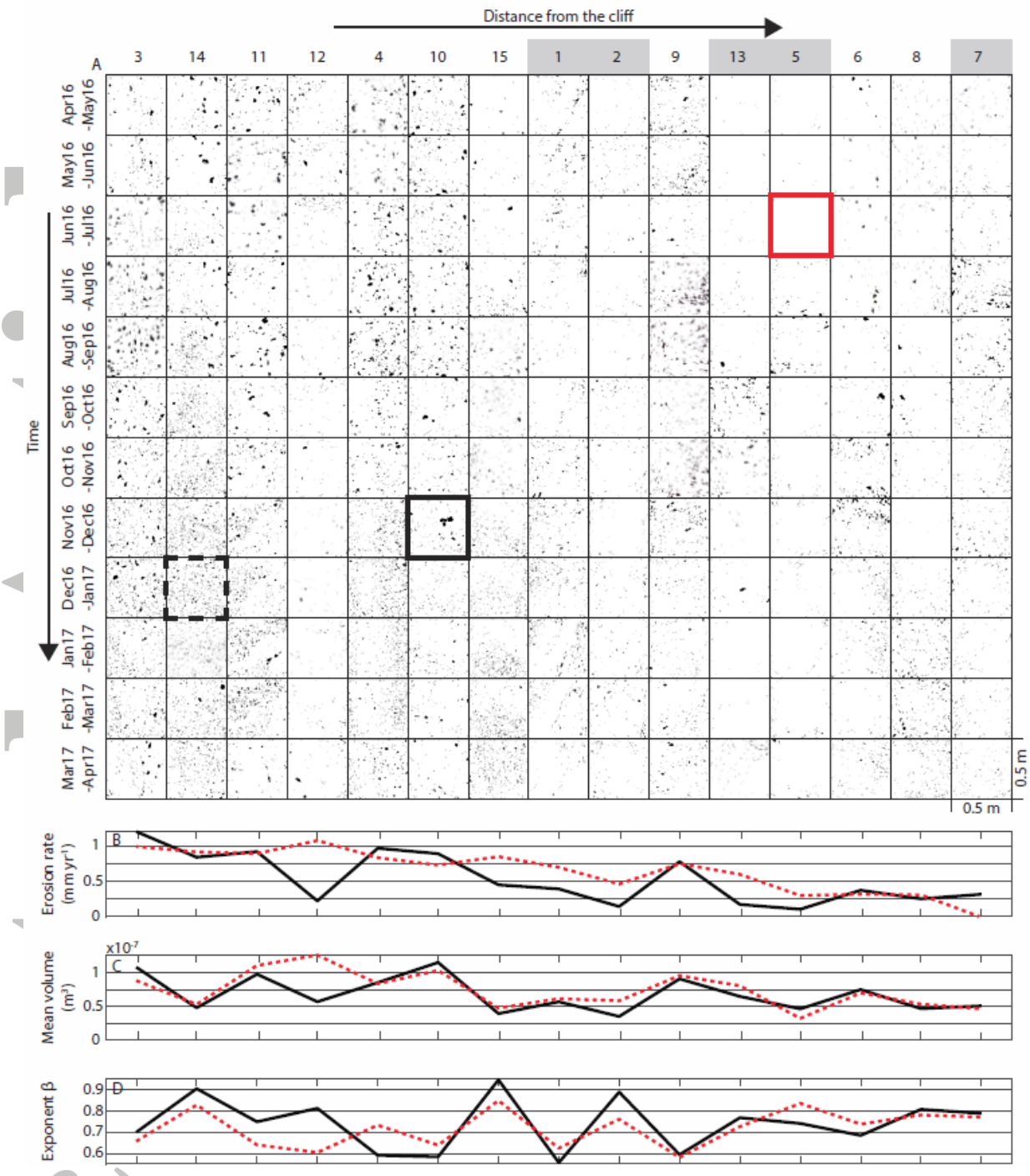

Figure 8. A) Monthly distribution of the detachments at the monitoring sites ordered by the distance from the cliff. Black polygons within each monitoring plot represent detachments. Sandstone sites are indicated by grey boxes, the remaining sites are located on shale sections of the platform. Grid cells with bold outlines represent example cells showing different modes of detachment. The solid black outline demonstrates an example of a large detachment with multiple smaller detachments.

The black dashed outline exemplifies a monitoring plot with multiple small detachments. The red outlined plot provides an example of where minimal erosion occurred during the monitoring period. Plots B, C and D illustrate how observed (black line) and model-predicted (red dashed line) erosion rate (B), mean volume (C) and β (D) vary with distance from the cliff.

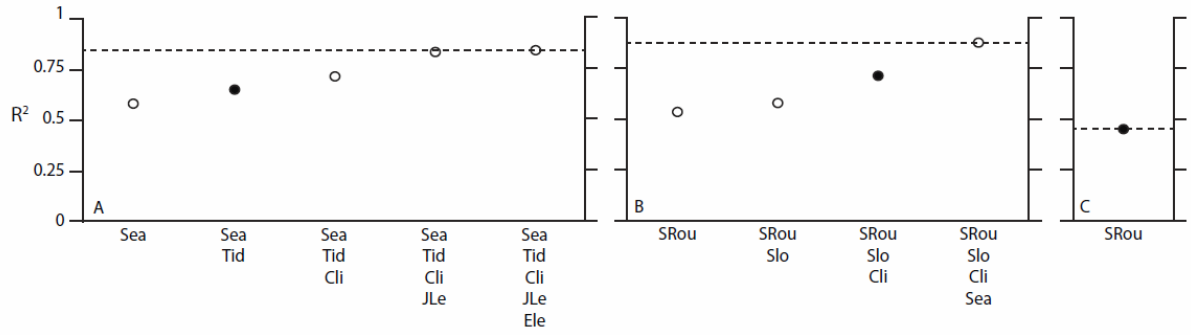

Figure 9. Sequence of input independent variables and resulting R^2 values ($p < 0.05$): A) Erosion rate, *Ero* (mm yr^{-1}); B) Mean volume, *Mean* (m^3); C) Exponent β; dashed lines represent maximum R^2 of the regression model when all variables are included. The accepted model is indicated by the black-filled circle.

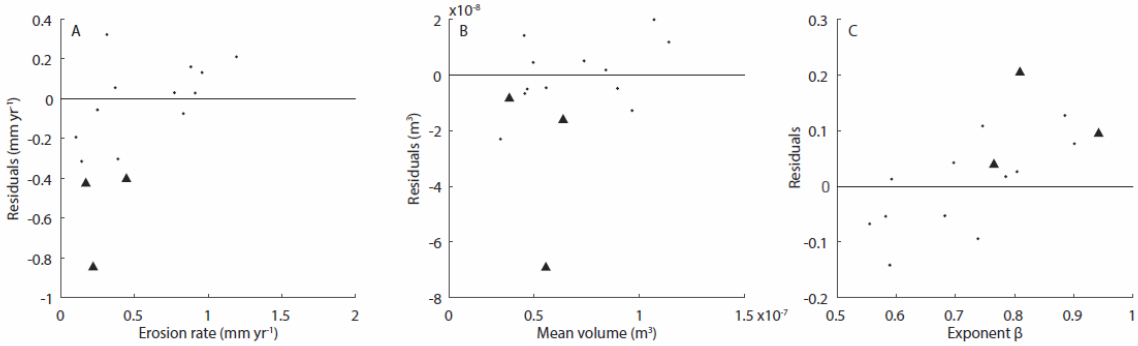

Figure 10. Distribution of residuals for the erosion variables: A) Erosion rate, *Ero* (mm yr^{-1}); B) Mean volume, *Mean* (m^3); C) Exponent *β*. Points represent the training set, triangles represent the test set; residuals are calculated as observed - predicted values.

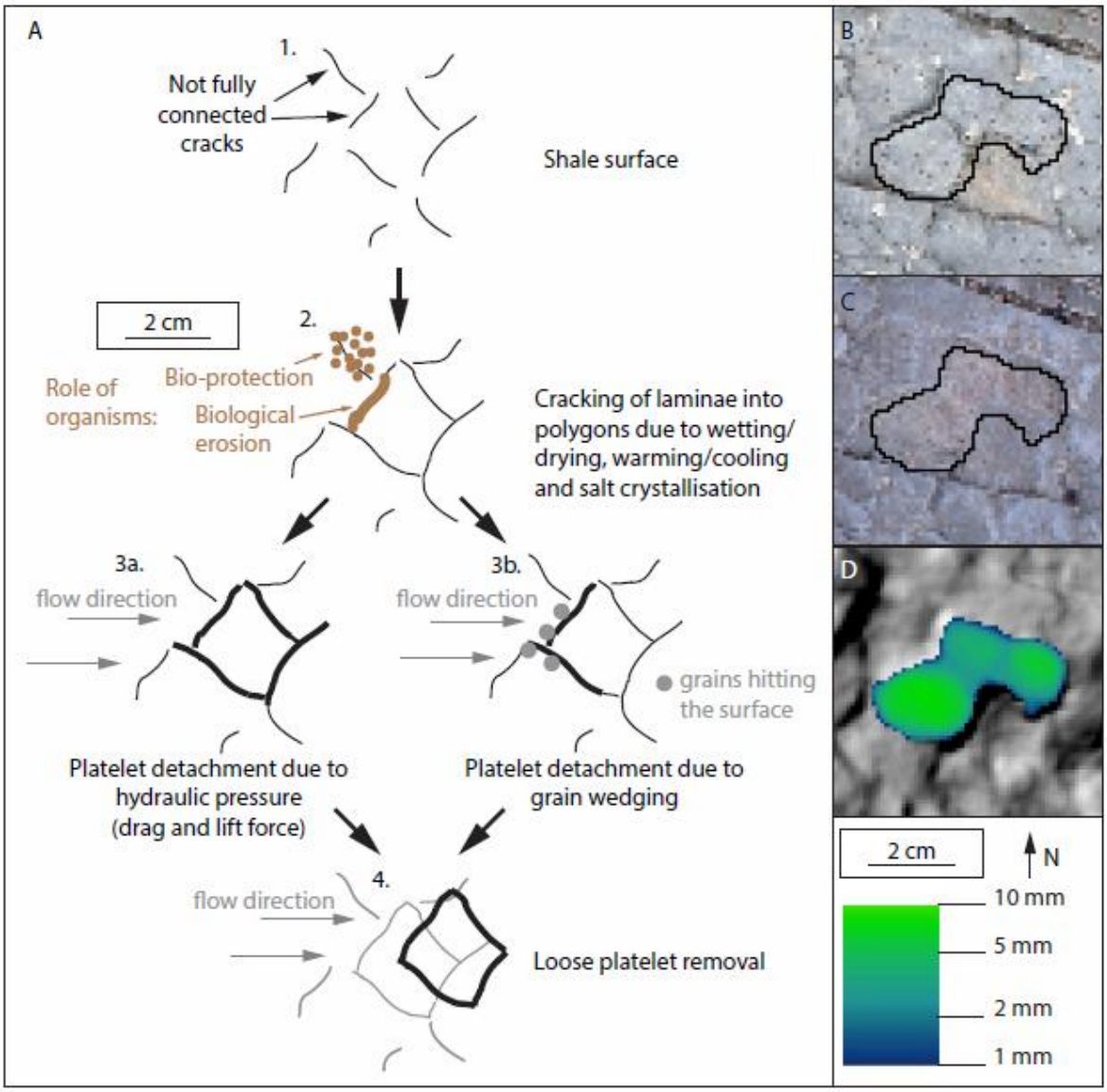

Figure 11. Schematic summary of the process of platelet detachment: A) conceptual model of detachment; the importance of biological activity is not explored in this study, but is notionally presented here in terms of the locations where bio-protection and biological erosion could feasibly occur, based on field observations; B-D: an example of detachment occurred in April-May 2016 at site 9: B) detachment outline with April 2016 ortho-photograph as background; C) detachment outline with May 2016 ortho-photograph as background; D) detachment thickness (common logarithmic scale) with April 2016 hillshade as background.